Intrinsic Nanoscale Structure of Thin Film Composite Polyamide Membranes: Connectivity, Defects, and Structure-Property Correlation

Xiaoxiao Song [a, b*], Bowen Gan [a], Saren Qi [c], Hao Guo [d], Chuyang Y. Tang [d*], Zhou Yong [a, b], Congjie Gao [a, b]

[a] Centre for Membrane Separation and Water Science & Technology, Department of Chemical Engineering, Zhejiang University of Technology, Hangzhou, 310014, P. R. China

[b] Collaborative Innovation Center of Membrane Separation and Water Treatment of Zhejiang Province, Hangzhou 310014, China

[c] Suzhou Institute of Nano-Tech and Nano-Bionics (SINANO), Chinese Academy of Sciences, Suzhou 215123, P. R. China

[d] Department of Civil Engineering, the University of Hong Kong, Pokfulam, Hong Kong SAR, P. R. China

[*] Corresponding Authors.

Xiaoxiao Song Tel: +86 (0571) 8832 4135, E-mail address: songxiaoxiao@zjut.edu.cn

Chuyang Y. Tang Tel: +852 2859 1976, Fax: +852 2559 5337, E-mail address: tangc@hku.hk

21 **TABLE OF CONTENTS**

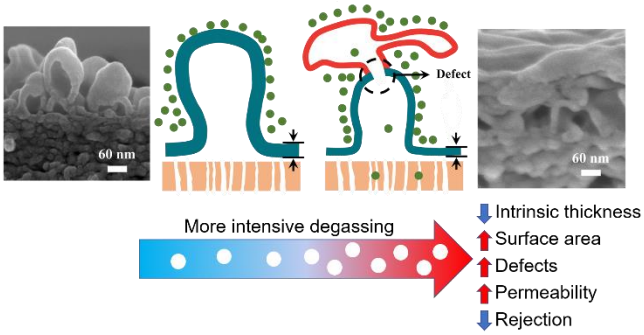

22

ABSTRACT

Transport of water, solutes, and contaminants through a thin film composite (TFC) membrane is governed by the intrinsic structure of its polyamide separation layer. In this work, we systematically characterized the nanoscale polyamide structure of four commercial TFC membranes to reveal the underlying structure-property relationship. For all the membranes, their polyamide layers have an intrinsic thickness in the range of 10 - 20 nm, which is an order of magnitude smaller than the more frequently reported apparent thickness of the roughness protuberances due to the ubiquitous presence of nanovoids within the rejection layers. Tracer filtration tests confirmed that these nanovoids are well connected to the pores in the substrates via the honeycomb-like opening of the backside of the polyamide layers such that the actual separation takes place at the frontside of the polyamide layer. Compared to SW30HR and BW30, loose membranes XLE and NF90 have thinner intrinsic thickness and greater effective filtration area (e.g., by the creation of secondary roughness features) for their polyamide layers, which correlates well to their significantly higher water permeability and lower salt rejection. With the aid of scanning electron microscopy, transmission electron microscopy, and tracer tests, the current study reveals the presence of nanosized defects in a polyamide film, which is possibly promoted by excessive interfacial degassing. The presence of such defects not only impairs the salt rejection but also has major implications for the removal of pathogens and micropollutants.

INTRODUCTION

Reverse osmosis (RO) is the method of choice for seawater desalination and potable water reuse.[1-3] Commercially available RO membranes are prepared from an interfacial polymerization (IP) reaction between *m*-phenylene diamine (MPD) and trimesoyl chloride (TMC). These membranes have a thin film composite (TFC) structure in which a thin and water-permeable polyamide (PA) rejection layer is supported by a porous substrate.[3-6] The PA rejection layer exhibits a "ridge-and-valley" surface roughness,[7-9] and the protuberances of roughness structures extend from a few tens to hundreds of nm away from the membrane surface.[10, 11] Consequently, some early studies report an (apparent) thickness in the range of ~ 50 to 300 nm for the rejection layer.[12-15]

Advanced microscopic characterization coupled with mechanistic investigation in recent years has significantly improved our understanding on the structure of the PA rejection layer.[3, 14, 16-22] For example, transmission electron microscopy (TEM) reveals the presence of a large fraction of nanovoids inside this layer,[3, 17-19, 23] such that its true thickness[19, 20, 24-27] would be an order of magnitude lower than the apparent thickness reported in earlier studies. More recent works[17, 28-30] have shown that the backside of the PA layer presents numerous honeycomb-like openings. According to Tang and coworkers,[23, 30-32] both the nanovoids and the honeycomb-like openings originate from degassing of CO_2 nanobubbles under the combined action of heat and H^+ generated by the IP reaction. The degassed nanobubbles are encapsulated by the PA film at the reaction interface to form the nanovoids, and their subsequent escape from porous

substrate leaves the honeycomb-like openings at the backside of the PA film.[30] Adding $NaHCO_3$, a CO_2 precursor, to the aqueous MPD solution resulted in larger roughness protuberances.[31] In contrast, removal of CO_2 from the MPD solution before the IP reaction eliminated the formation of "ridge-and-valley" surface roughness.[23]

Despite the apparent importance of these morphological features (the PA film thickness,[19, 24, 25, 27, 33] its surface roughness,[30, 34-36] and its void fractions,[19, 31, 37-39] etc.) on the properties of TFC RO membranes, a number of critical issues remain to be systematically addressed. For example, recent works based microscopic characterization and tracer tests have provided evidences of pore connectivity within PA films,[19, 22] yet its underlining mechanism needs to be further investigated. Another critical question is whether the PA rejection layer is prone to the formation of defects. Ideally, the free volume pores (~ 0.2 nm in radii[7, 40]) in RO membranes should be small enough to completely remove viruses and bacteria. Nevertheless, incomplete and often disparate removal data have been reported for intact membrane elements (e.g., 5 to 7 log removal for the MS2 virus of ~25 nm in size;[41, 42] 3 to ≥4 log removal for a DNA of ~71 nm in size;[43] and 6.8-6.9 log removal for bacteria surrogates of ~500 nm in size [44]). In addition to issues related to membrane modules (e.g., failure of glue lines), could the structure of polyamide film inherently affect the integrity of the membrane?

Motivated by these questions, the current study aims to establish the structure-properties relationship and its underlying mechanisms for TFC membranes. The

morphological features of four commercial PA membranes were thoroughly characterized and correlated to their permeability and rejection properties. Additional tracer filtration tests were designed to reveal the membrane connectivity and defect location. The results of this study not only provide fundamental insights to the transport properties of RO membranes but also have critical implications to their synthesis and environmental applications.

EXPERIMENTAL

Chemicals and materials

Humic acid (HA) was purchased from Sigma-Aldrich (H16752, technical grade, St. Louis, MO). N,N-dimethylformamide (DMF), Sodium Chloride (NaCl), Sodium hypochlorite (NaOCl), Ferric (II) sulfate ($FeSO_4$, or Fe(II)) were supplied by Aladdin (Shanghai, China). Four commercial TFC PA membranes, including a seawater RO membrane SW30HR, two brackish water RO membranes BW30 and XLE, and a nanofiltration membrane NF90, were all obtained from Dow Filmtech™ (Minneapolis, MN).[45] All these membranes have a fully aromatic PA chemistry, formed based on the reaction between MPD and TMC.[46, 47] Compared to SW30HR and BW30, XLE and NF90 are known as "loose" PA membranes[47] with significantly higher water permeability but lower NaCl rejection (Table 1). In addition to the commercial TFC PA membranes, a polysulfone (PSF) ultrafiltration membrane (Aromem Pte. Ltd., Suzhou, China) was used as a control for the membrane chlorination treatment.

Table 1. Separation properties and structural characteristics of the commercial TFC membranes (all data obtained from the current study)

Membrane		SW30HR[c]	BW30	XLE	NF90
Separation performance at low salinity[a]	Water flux, J (L m^{-2} h^{-1})	9.0 ± 0.8	61.4 ± 2.6	101.8 ± 1.4	125.4 ± 1.0
	Salt rejection, R (%)	98.5 ± 0.2	96.9 ± 0.3	92.6 ± 0.5	83.8 ± 0.3
Separation performance at high salinity[b]	Water flux, J (L m^{-2} h^{-1})	18.9 ± 1.7	95.4 ± 0.7	120.0 ± 0.9	125.0 ± 1.3
	Salt rejection, R (%)	99.4 ± 0.1	97.4 ± 0.3	92.1 ± 0.5	84.3 ± 0.2
Pores on substrate	Diameter, d_p (nm)	15.2 ± 4.8	9.1 ± 1.9	15.5 ± 3.8	13.1 ± 5.0
	Number density (counts/μm^2)	439	872	525	932
	Area coverage (%)	11.6	5.9	10.9	14.5
Openings on PA backside	Diameter, d_o (nm)	39.1 ± 12.4	52.9 ± 16.0	51.5 ± 17.1	38.6 ± 10.4
	Number density (counts/μm^2)	168	106	158	142
	Area coverage (%)	27.1	25.4	47.5	22.9
Nodule size d_n, measured by SEM (nm)		46.7 ± 14.5	60.2 ± 9.5	84.8 ± 27.7	67.1 ± 13.8
d_n/d_o ratio		1.2	1.1	1.6	1.7
Average roughness R_a (nm)[e]		48.8 ± 2.5	36.0 ± 1.4	61.4 ± 1.8	50.6 ± 7.1
Root Mean Square (RMS) roughness R_q (nm)[e]		60.6 ± 3.5	45.6 ± 2.3	77.6 ± 3.5	66.8 ± 9.3
Maximum roughness R_{max} (nm)[e]		425 ± 59	355 ± 38	560 ± 34	540 ± 93
Surface area ratio (SAR), measured by TEM (-)[d]		3.35	3.78	7.05	5.62
SAR, measured by AFM (-)[e]		1.290	1.341	1.329	1.252
δ_{app}, measured by TEM (nm)[d,f]		129 ± 61	118 ± 58	277 ± 43	159 ± 27
δ_{app}, measured by AFM (nm)[e,g]		169 ± 11	112 ± 16	204 ± 24	122 ± 8
δ_{int} (nm)[d]		17.4 ± 2.0	17.8 ± 1.9	13.9 ± 1.8	11.8 ± 1.7

a. Brackish water desalination testing conditions: 1.6 MPa, 2000 ppm NaCl, 25 ± 1 ˚C. Refer to Supporting Information S1 for more detailed testing information.

b. Seawater desalination testing conditions: 5.5 MPa, 32000 ppm NaCl, 25 ± 1 ˚C. Refer to Supporting information S1 for more detailed testing information.

c. The condition duration was 24 hours for SW30HR and 1 hour for the other 3 membranes.

d. Based on TEM characterization.

e. Based on atomic force microscopy (AFM) characterization.

f. The apparent thickness, δ_{app}, was obtained from TEM images by sampling at different locations (see Figure S4 in Supporting Information S5).

g. The apparent thickness, δ_{app}, was calculated based on the average height of isolated polyamide films by AFM measurements (Figure 2).

Isolation of PA rejection layer and PSF substrate

To obtain isolated PA rejection layer from a TFC membrane, its PSF substrate was dissolved by pure DMF.[15, 30] The isolated PA layer was picked up from the DMF solution by a stainless steel washer, transferred to a silicon wafer, and then further treated by three cycles of DMF rinsing (3 min) and soaking (10 mins) to remove any residual PSF. The treated sample was kept in a vacuum dryer for further characterization.

For the isolation of the PSF substrate, the PA layer of the TFC membrane was removed by washing with 1% NaOCl solution at pH 12 for 15 hours. The combination of high hypochlorite concentration and high pH is known to completely degrade the PA layer.[48] At the same time, controlled experiment of NaOCl treatment for the PSF ultrafiltration membrane under identical conditions did not result in significant changes of its pore size distribution and pure water permeability (Supporting Information S2). Therefore, the NaOCl treatment in the current study is expected to remove the PA layer while preserving the pore structure of the substrate.

Microscopic characterization

The surface morphology and cross-sectional structure of the membranes were characterized by an ultrahigh-resolution field-emission scanning electron microscope (FESEM, Hitachi SU8010, Japan). Membrane cross-sections were produced by fracturing membrane coupons in liquid N_2. In addition, FESEM characterization was also performed for PA rejection layers and PSF substrates isolated from the commercial

TFC membranes. Prior to FESEM observation, the samples were sputter coated with Pt at a coating distance of ~ 8 cm with a current of 15 mA. The coating time for membrane front surface and cross-section was 30 and 45 s, respectively. A shorter coating time of 20 s was used for the backside of the isolated PA layer as well as the front surface of the isolated PSF substrate to minimize the impact of Pt deposition on the determination of pore size.

Cross-sectional TEM images were acquired with a JEM1200EX TEM (acceleration voltage of 80 kV, JOEL, Tokyo, Japan). Membrane samples were dehydrated gradually in a series of ethanol/water solution (0%, 25%, 50%, 75%, and 100% ethanol content, each step for 5 minutes) and subsequently embedded in LR White Resin (London Resin Company, Reading, UK). The resin-embedded membrane samples were sliced into ultrathin sections of ~ 80 nm using a Leica EM UC7 (Leica Microsystems, Wetzlar, Germany).[23, 46] An AFM (ICON, Bruker, Billerica, MA) was used to obtain the topological images of isolated PA layers of SW30, BW30, XLE, and NF90 (placed on a silicon wafer) using a tapping mode.[30]

Tracer filtration tests

Tracer filtration tests (also known as penetration tests in some earlier studies[49]) were performed for BW30 and NF90 in a customized filtration cell (effective filtration area of ~ 19.6 cm^2) to assess the interconnectivity within the PA layer and to determine the location where separation takes place. HA was chosen as a tracer in this study due to its

168 good solubility and low cost. Its small size (~ 1.1 – 5.4 nm [50]) and soft nature may allow
169 it to better penetration into pores and defects compared to rigid silver or gold
170 nanoparticles.[8, 22, 49, 51] For a typical test, a virgin membrane was operated in the "reverse
171 orientation" with its substrate side exposed to the feed solution (a 5 mg/L HA solution)
172 under a constant pressure of 0.69 MPa (i.e., 100 psi) for 96 hours. Such a tracer test in
173 the "reverse orientation" allows HA macromolecules to access the backside of the PA
174 layer. Additional HA tracer tests were performed in the "normal orientation" to allow
175 HA macromolecules to access the frontside of the PA layer (see more details in
176 Supporting Information S8). As a complimentary test to the pressure-driven tests, an
177 osmotically driven filtration test was also performed using NaCl as draw solution and
178 Fe (II) as a tracer (Supporting Information S7) with the backside of the PA layer exposed
179 to the tracer.
180
181 **RESULTS AND DISCUSSION**
182 ***Morphology of PA rejection layers***
183 The micrographs of membrane top surfaces and cross-sections are presented in Figure
184 1a. The surfaces of SW30HR and BW30 have a "ridge-and-valley" appearance that is
185 characterized by the presence of numerous nodules and leaves.[8, 17, 47 11, 52] Their cross-
186 sectional FESEM and TEM micrographs show a basal layer of nanovoid-containing
187 nodular and leave-like features that are densely packed side by side. According to our
188 previous studies,[23, 30] the nodular features originate from the interfacial degassing of
189 CO_2 nanobubbles during the IP reaction that are subsequently encapsulated by the PA

layer. On the other hand, the dehydration of larger nodules causes them to collapse into a leaf-like appearance during membrane drying.[30] For these reasons, this basal layer is termed as the "nodular layer" in the current study.

XLE and NF90, both considered as loose TFC PA membranes with high permeability and low NaCl rejection (Table 1),[47] present substantially different PA morphology that is characterized by a dual-layer structure with a basal nodular layer overlaid by an additional exterior layer (see the FESEM and TEM cross-sections in Figure 1a). Based on the FESEM surface micrographs, the exterior layer consists largely interconnected and relatively flat features (Supporting Information S3). This exterior layer covers substantial fraction of the surface, leaving some crater-like regions with the underlying basal nodular features exposed. The exterior layer could not be removed by DMF washing or long-term filtration operation, confirming that this layer is firmly connected to the basal layer. Additional analysis (Supporting Information S4 and Table 1) shows that average size of the nodules (d_n) following the order of XLE (84.8 ± 27.7 nm) > NF90 (67.1 ± 13.8 nm) > BW30 (60.2 ± 9.5 nm) > SW30HR (46.7 ± 14.5 nm). The unique dual layer roughness structure of XLE and NF90 (Figure 1b) may be explained by more favorable CO_2 degassing during their interfacial polymerization. Previous studies reported the formation of larger nodules due to improved CO_2 degassing.[31, 32] Indeed, dosing 2-6 wt.% $NaHCO_3$ (a CO_2 precursor) into the MPD monomer solution led to the formation of a dual layer structure with similar appearance to those of XLE and NF90.[31]

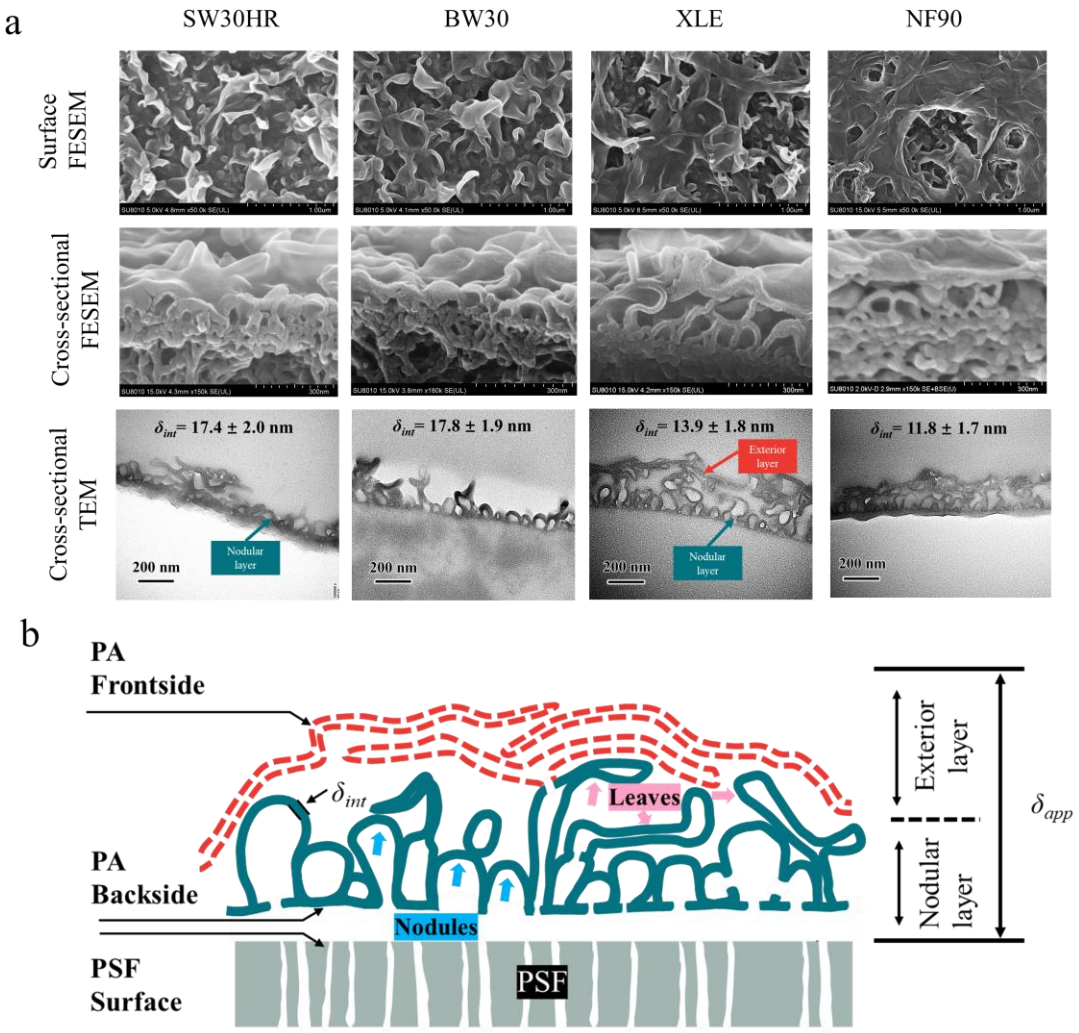

Figure 1. (a) The surface FESEM, cross-sectional FESEM, and cross-sectional TEM images of SW30HR, BW30, XLE, and NF90 membranes; (b) The schematic illustration of a PA layer featuring a dual layer structure, with a basal nodular layer composed of tightly packed nodules (represented by the green solid lines) and an exterior layer composed of interconnected flat features (represented by the red dotted lines). The dual layer structure was observed in XLE and NF90 membrane, but not in BW30 and SW30HR membrane.

Apparent thickness, intrinsic thickness, and effective filtration area of PA layers

The apparent thickness (δ_{app}) of the PA layers, measured from the cross-sectional TEM images (Figure 1a and Figure S4a in Supporting Information S5), followed the order of XLE (277 ± 43 nm) > NF90 (159 ± 27 nm) > SW30HR (129 ± 61 nm) > BW30 (118 ± 58 nm). AFM height analysis provides an alternative measurement of δ_{app} based on the height histogram (Figure 2). Due to the existence of the additional exterior layer, the δ_{app} values of XLE (204 ± 24 nm) and NF90 (122 ± 8 nm) were approximately double of their average nodular size. SW30HR and BW30 had apparent thicknesses of 169 ± 11 nm and 112 ± 16 nm, respectively, which were significantly larger than the average nodular size partially due to the presence of leaf-like features. Furthermore, the additional surface coating layer of polyvinyl alcohol (PVA) of these two membranes[46, 47] also result in over-estimations of δ_{app} values by the AFM method, since AFM is not able to differentiate PVA from PA.

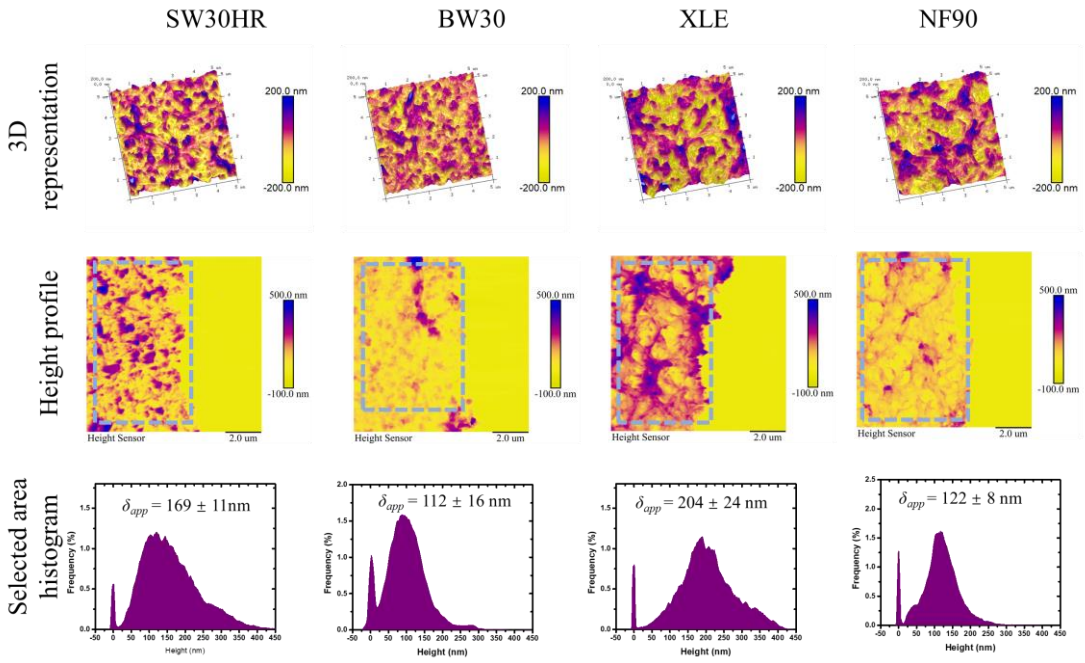

Figure 2. The AFM 3D representation, height profile, and selected area histograms of the isolated PA layers of SW30HR, BW30, XLE, and NF90 membranes.

The intrinsic PA thickness (δ_{int}, Figure 1b and Table 1) was estimated from the cross-sectional TEM images (Figure 1a and Figure S4b in Supporting Information S5). For any given membrane, its nodules had relatively uniform intrinsic layer thicknesses in the range of 10 - 20 nm, which is in good agreement with the existing literature.[17, 24, 35, 53] Similar intrinsic thickness was also reported by Song et al.[19] for roughness nodules ("domes"). Using a quantitative electron tomography, these authors also found that "dimpled" and "clustered" crumples (which are possibly related to collapsed leaf-like features and the secondary layer reported in this study, respectively) could have greater film thickness. In the current study, XLE (13.9 ± 1.8 nm) and NF90 (11.8 ± 1.7 nm) had thinner δ_{int} compared to SW30HR (δ_{int} = 17.4 ± 2.0 nm) and BW30 (17.8 ± 1.9 nm), which partially explains the greater water permeability of the loose XLE and NF90 membranes (Table 1). This finding also underpins the recent attempts of making thinner PA rejection layer in order to achieve higher membrane water permeability.[23, 24, 33, 35, 54, 55]

Membrane water permeability is also greatly affected by the effective PA surface area,[23, 53] which is in turn affected by the membrane surface roughness features. The average surface roughness values (R_a, see Figure 2 and Table 1) of the loose membranes XLE and NF90 were 61.4 ± 1.8 nm and 50.6 ± 7.1 nm, respectively. Those of SW30HR and BW30 were 48.8 ± 2.5 nm and BW30 36.0 ± 1.4 nm, respectively. The SAR, i.e., the ratio of the three-dimensional (3D) surface area measured by AFM over its projected

plan area, had the following order (Table 1): BW30 (1.341) > XLE (1.329) > SW30HR (1.290) > NF90 (1.252). In the current study, neither R_a or SAR measured by AFM seems to provide satisfactory explanation to the ten-fold higher flux of the loose membranes (XLE and NF90) compared to SW30HR under the low salinity testing conditions (Table 1). This is due to the inherent limitation of AFM measurement that only the front (exposed) area can be accessed by its tip of finite size.[31]

In comparison to the AFM data, the SAR values obtained from TEM cross-sections (Supporting Information S6 and Table 1) were substantially larger. For example, the SAR value of SW30HR estimated from the 2D TEM image analysis was 3.35, which was much larger than the AFM-based SAR of 1.290. A similar trend has been observed by Culp et al.[21]. Furthermore, the SAR value obtained in this study agrees reasonably well with the value obtained from the 3D TEM tomography[21] (3.35 vs. 3.48 for SW30HR), suggesting that the 2D image analysis described in this study could offer a simpler alternative to the more sophisticated 3D approach. Compared to SW30HR and BW30, loose membranes XLE and NF90 had much larger SAR values (Table 1), which is attributed to the additional area contributed by the exterior layer. For example, the SAR values of XLE estimated from its TEM cross-section (Supporting Information S6) was as large as 7.05. Our result is also consistent with the 3D TEM measurements by Song et al.[19], who reported that the localized SAR varied from 3.5 to 15.7 for a polyamide film synthesized on a sacrificial layer. Compared to AFM measurements, the TEM-based SAR provides better explanation to the significantly higher water

permeability of the loose PA membranes.

Hierarchical pore structure and interconnectivity within the PA layer

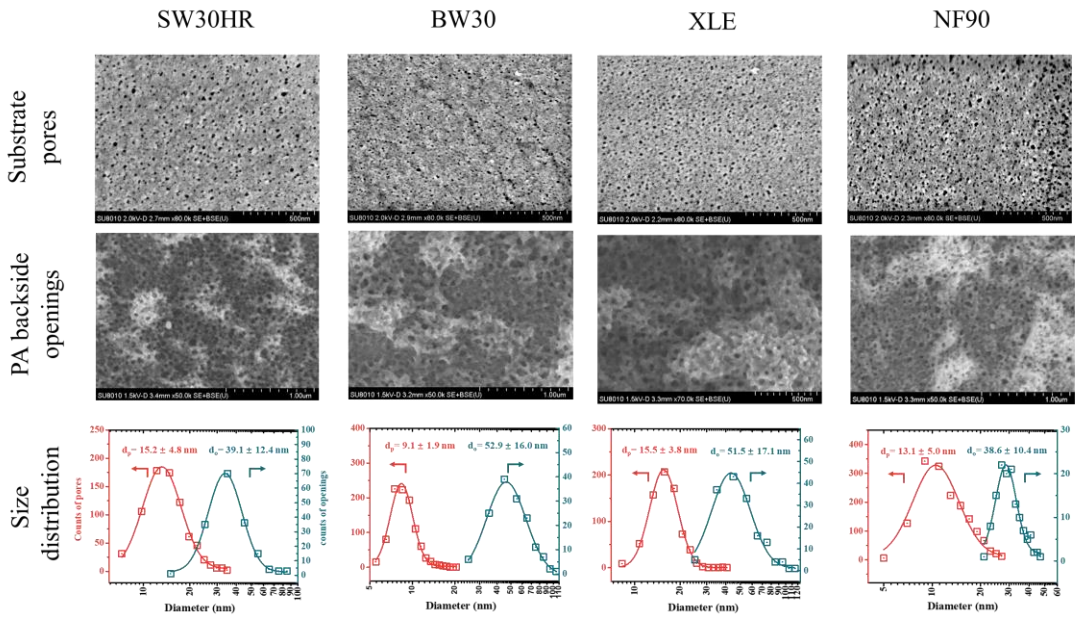

Figure 3. FESEM micrographs and pore size distributions of the PSF substrates and the backside openings of the PA rejection layer. To isolate the PSF substrate, the PA layer of the TFC membrane was removed using 1% NaOCl solution at pH 12. On the other hand, the PA rejection layer was isolated by dissolving the PSF substrate in DMF. For the size distribution curves, the red and green curves correspond to the pore sizes on the polysulfone surface and polyamide backside, respectively.

Figure 3 shows FESEM micrographs of the membrane substrates and the backsides of PA layers. The backside of all the membranes features honeycomb-like openings, with the opening density in the range of 100 to 200 counts/μm^2 and the average opening diameter (d_o) in the range of 39 to 53 nm (Figure 3 and Table 1). These data agree reasonably well with previous studies.[17, 28, 30] Based on FESEM and TEM cross-

sectional micrographs (Figure 1) and previous studies[22, 30], we hypothesize that the openings in the backside are directly connected to the nanovoids in the PA layer. Meanwhile, the density of the substrate pores (in the range of 439 to 932 counts/μm^2) was 2.6 - 8.2 times of that of the PA backside openings for the corresponding membrane, suggesting that each opening may be connected to multiple pores in the substrate.

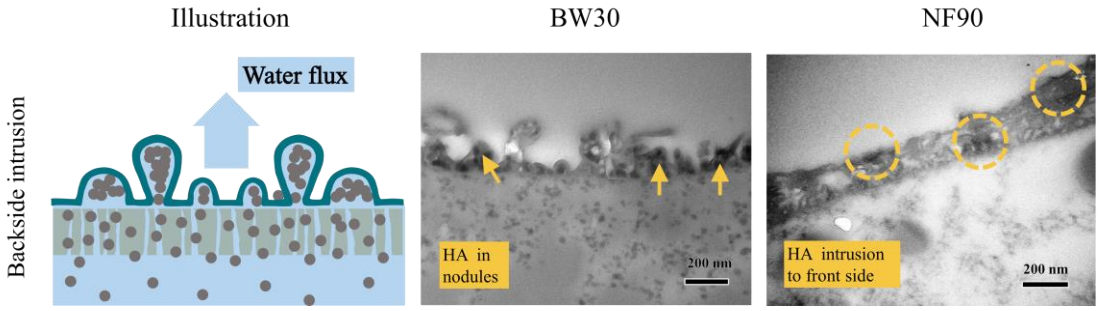

Figure 4. The illustration of HA tracer test from the backside of the PA layer (left panel) and TEM micrographs of BW30 and NF90 after the HA tracer test (right panel).

In order to further study the connectivity within the hierarchical pore structure, we performed tracer filtration tests for BW30 and NF90 from the substrate side using HA as a molecular tracer (Figure 4). The macromolecular nature of HA (approximate size range from 1.1 – 5.4 nm [50]) allows it to penetrate through pores and defects but not an intact PA film. For both membranes, HA was able to reach all the way to the nanovoids within the PA layer. Our observation is consistent with Li et al.[22] who reported the penetration of 1-nm gold nanoparticles into the interior of polyamide nodules. An additional test was also performed using $FeSO_4$ as a tracer on the backside of a PA layer isolated from BW30 using an osmotically driven water permeation, which led to the accumulation of iron hydroxide deposition within the nodular structures (Supporting

317 Information S7). Earlier studies believe that separation of solutes occurs at a "dense
318 base" of the PA layer.[8, 9] Nevertheless, the observation of honeycomb-like openings at
319 its backside (Figure 3) and the ability of both HA and $FeSO_4$ tracers to access nanovoids
320 in the roughness nodules (Figure 4 and Supporting Information S7) provide strong
321 evidence that the actual separation takes place at the frontside of the PA layer instead
322 of its backside.
323
324 Tracer tests by HA from the frontside was also performed for BW30 and NF90
325 (Supporting Information S8). For the tight BW30 membrane, HA deposited above the
326 nodules/leaves of the PA layer, whereas the nodular voids within the PA layer and the
327 pores in the substrate were largely free of HA. For the loose NF90 membrane, large
328 amount of HA particles deposited in the gap between its exterior layer and nodular layer
329 of the roughness structure. Moreover, some HA particles penetrated through the nodules
330 and deposited within their nanovoids. A tiny fraction of HA even reached the pores of
331 the substrate (marked by the red arrows in Figure S8). We further compared the
332 rejection of HA by NF90 and BW30. While HA was found in the permeate of NF90, it
333 was below the detection limit in the permeate of BW30 (Figure S9, Supporting
334 Information S8). These results suggest the possible presence of defects in the PA layer
335 of NF90. On the other hand, the better integrity of BW30 may be attributed to a more
336 intact polyamide film and/or its PVA surface coating[46]. Additional high resolution
337 FESEM micrographs of NF90 (Figure S10) reveal the frequent existence of nanosized
338 holes of 10-50 nm in size on the nodular walls of its PA layer. These holes can provide

interconnectivity between adjacent nodules.[19] If not completely enclosed during the film growth, they could also potentially lead to defects through the PA layer. The possible existence of defects within the PA rejection layer, in addition to integrity of glue lines in membrane modules, may explain the incomplete removal of viruses whose physical sizes (e.g., of several tens of nm) are several orders of magnitude larger than the pore size of RO membranes.[42] It also provides insights to the observation that a series of RO membranes, even though having similar PA network pore-volumes, can exhibit significantly different rejection rates to small neutral solutes.[56] Furthermore, it is consistent with the observation that membrane rejection can be significantly improved under mild/initial fouling by macromolecules thanks to the partial sealing of defects.[57]

Mechanistic insights of roughness structures, inter-connectivity, and defects formation of PA layers

Figure 5 presents a schematic diagram to illustrate the mechanisms involved in forming the roughness structures as well as defects of PA layers. During the IP reaction, MPD and TMC react rapidly to form oligomers (Stage I) and eventually a nascent cross-linked network of polyamide (Stage II). CO_2 nanobubbles released during IP and confined between the substrate and the nascent PA film lead to the formation of "balloon-like" nodular roughness features,[23, 30, 31] while the thickness of the PA film can be strongly affected by the reaction recipe (e.g., monomer concentrations[26, 27, 33]). The release of gas nanobubbles can also potentially lead to convection of monomer

361 solutions, which can further influence the integrity as well as the final shape of the PA
362 layer (Stage III). For example, when the PA layer completely encapsulates CO_2
363 nanobubbles, a defect-free dense RO membrane is expected (Figure 5, Scenario 1).
364 However, in some cases, the gas bubble may start to escape from a nascent PA nodule
365 before it completely encapsulates the gas bubble. This escape of the bubble drives the
366 convection of the MPD solution towards the TMC solution, which promotes the
367 formation of secondary structures such as a secondary nodule (or "grafted" nodule) that
368 is well connected to the primary nodule (Scenario 2). Under conditions where rigorous
369 degassing prevails, the escape of the gas bubble can be so forceful that the reaction
370 frontier assumes a shape similar to a pressurized water jet instead of the common
371 balloon-like shape, which is responsible for the formation of the exterior layer with a
372 large aspect ratio of length/width (Scenario 3). Extremely forceful degassing and/or the
373 depletion of MPD monomers may further result in the formation of defects such as the
374 incomplete enclosure of the primary nodules (Scenario 4). In reality, a combination of
375 the various scenarios can be applicable to the same membrane (e.g., the observation of
376 all the four scenarios for NF90), which can be attributed to the highly heterogeneous IP
377 reaction conditions at the nanoscale.
378

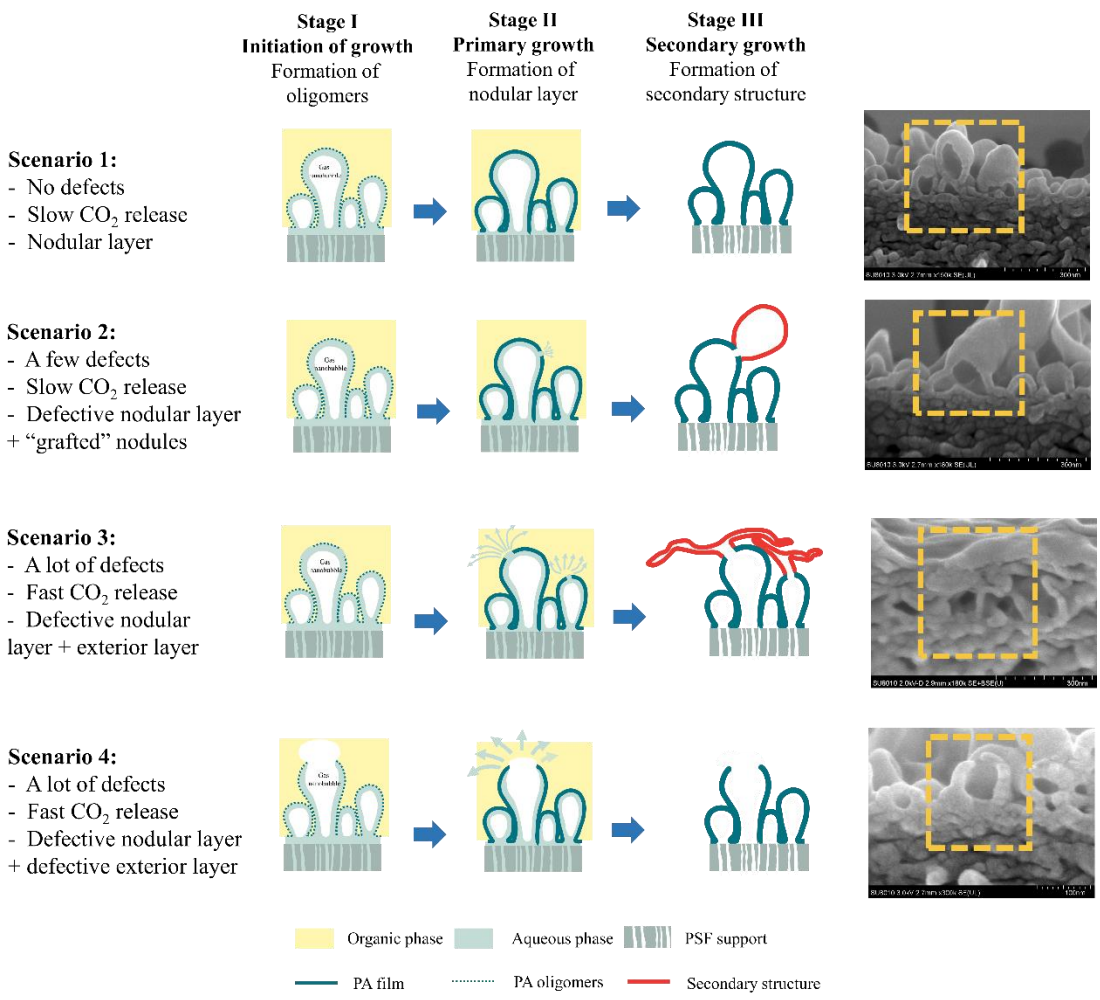

379

380 **Figure 5.** Formation mechanisms of the nodular layer and the exterior layer.

381

382 In the current study, we performed XPS elemental composition analysis of both the
383 frontside and backside of PA layers isolated from NF90 and XLE (Table S1). The O/N
384 ratios of the frontside of XLE (1.50) and NF90 (1.36) were much higher than the
385 respective values of the backside (1.07 for XLE and 1.01 for NF90), revealing that the
386 cross-linking degree of the exterior layer was much lower compared to that of the
387 nodular layer.[46] In contrast, tight RO membranes have been reported to have more
388 uniform chemical compositions across their PA layers.[58] The large difference in the O/N
389 ratios between of front and back sides for the loose membranes XLE and NF90 supports

390 our explanation of the formation of exterior layer due to gas escape from the primary
391 nodules. That is, the forced convention of the MPD solution into the TMC solution
392 would induce a more TMC-rich and MPD-lean environment, which would in turn form
393 less crosslinked[6, 13] secondary PA structure in good agreement to our experimental
394 observation. Interestingly, Table 1 shows that the d_n/d_o ratios, representing the relative
395 size of nodules over that of backside pore openings, of the loose membranes XLE (1.6)
396 and NF90 (1.7) were significantly greater than those of the tight membranes SW30HR
397 (1.2) and BW30 (1.1). This observation is consistent with the possibly more intensive
398 degassing during the formation of the loose membranes.
399

Table 2. Correlation coefficients of key measured parameters of commercial RO membranes.[a]

		J **(Brackish)**	***R*** **(Brackish)**	**Pore diameter**	**Pore density**	**Pore coverage**	**Opening diameter**	**Opening density**	**Opening coverage**	d_n	R_a	**SAR (AFM)**	**SAR (TEM)**	δ_{app}	δ_{int}
J **(Brackish)**		1													
R **(Brackish)**		**-0.88**	1												
Substrate Pore	**Diameter**	-0.04	-0.09	1											
	Density	**0.58**	**-0.58**	**-0.76**	1										
	Coverage	0.37	**-0.69**	**0.68**	-0.08	1									
Opening	**Diameter**	0.11	0.36	-0.42	0.05	**-0.80**	1								
	Density	-0.19	-0.01	**0.98**	**-0.78**	**0.68**	**-0.53**	1							
	Coverage	0.21	0.11	**0.54**	**-0.56**	-0.03	**0.53**	0.40	1						
Nodule size, d_n		**0.79**	-0.47	0.20	0.08	0.11	**0.51**	0.01	**0.76**	1					
R_a		0.38	-0.35	**0.88**	**-0.52**	**0.63**	-0.13	**0.78**	**0.75**	**0.64**	1				
SAR (AFM)		-0.25	**0.67**	-0.33	-0.22	**-0.88**	**0.93**	-0.39	**0.50**	0.24	-0.20	1			
SAR (TEM)		**0.81**	**-0.60**	0.42	0.00	0.39	0.24	0.24	**0.72**	**0.96**	**0.80**	-0.02	1		
δ_{app}		-0.11	0.23	**0.85**	**-0.87**	0.23	0.12	**0.78**	**0.87**	0.42	**0.83**	0.22	0.49	1	
δ_{int}		**-0.88**	**0.95**	-0.35	-0.32	**-0.77**	0.31	-0.24	-0.17	**-0.63**	**-0.62**	**0.60**	**-0.78**	-0.09	1

a. The correlation coefficient R^2 was obtained using Microsoft Excel software. The correlation is classified in strongly correlated ($|R^2| \geq 0.8$), well correlated ($0.8 > |R^2| \geq 0.5$), weakly correlated ($0.5 > |R^2| \geq 0.3$), and no obvious correlation ($|R^2| < 0.3$). Bold font is used to indicate cases of strongly or well correlated cased.

Structure-property relationship

Table 2 shows the correlation among various parameters for the four TFC membranes. The salt rejection was strongly negatively correlated to the membrane water flux, which is expected based on the well-known upper bound theory describing the tradeoff relationship between membrane selectivity and permeance.[6, 59, 60] Among all the parameters, the intrinsic PA thickness had the strongest impact on the membrane separation properties, with a thinner δ_{int} resulting in a greater flux (R^2 = -0.88) but reduced NaCl rejection (R^2 = 0.95). In addition, greater effective filtration area (as characterized by the TEM-based SAR) also led to enhanced flux (R^2 = 0.81) and poorer NaCl rejection (R^2 = -0.60). The negative correlation between TEM-based SAR and NaCl rejection was likely due to the greater presence of defects in membranes containing extensive exterior layers. Compared to the intrinsic PA thickness and the TEM-based SAR, the more widely used conventional parameters including the apparent PA thickness and the AFM-based SAR were far less useful for the prediction of membrane separation properties. In the current study, the flux and rejection of the membranes also appeared to be correlated to the pore number density and coverage (i.e., surface porosity) of the substrate and the average nodular size. Our correlation analysis supports the earlier studies [30, 31] reporting the positive role of larger nodular size and greater surface roughness in enhancing membrane permeability by offering greater effective filtration area (see their strong correlation with TEM-based SAR in Table 2). The important role of the substrate revealed in this analysis also underpins the increased interest[61-63] in the optimization of the substrate pore structure. Based on the

observations in this study, the higher water permeability of the loose XLE and NF90 membranes can be mainly attributed to their thinner intrinsic PA thickness and larger effective filtration area, both resulting in reduced hydraulic resistance. On the other hand, the formation of a more defective PA film and the reduced crosslinking degree (e.g., for the exterior layer) are likely responsible for the reduced salt rejection. Despite the insights revealed by the correlation analysis, the readers need to be mindful that such analysis was only based on a limited collection of commercial membranes (4 types) with proprietary recipes. Furthermore, these commercial membranes were provided in their dry state, which could cause some deformation of morphological features.[30] Future studies need to expand the correlation analysis to a wider range of membranes, including samples synthesized under controlled synthesis conditions and without drying history.

Implications and perspectives

The current study suggests that the membrane transport properties are governed by a selective PA skin of 10-20 nm in intrinsic thickness. On the other hand, the backside of the PA rejection layer is porous and does not appear to contribute to solute rejection. The new mechanistic insights gained with respect to the intrinsic structure of the discriminative PA layer, its connectivity to the substrate pores and the structure-properties correlation facilitate improved understanding of transport phenomena in RO membranes. For example, the inherent tendency to form nanosized defects as a result of interfacial degassing during membrane formation has major implications to the

441 removal of pathogens and micropollutants, both of which are of critical concerns for
442 water reuse applications.[2] In this respect, additional studies of in-depth material
443 characterization and multi-scale simulations are needed. For example, RO membranes
444 are traditionally modelled by the solution-diffusion theory (which assumes diffusion is
445 the sole transport mechanism). Although some studies have included additional
446 convective transport of solutes across RO membranes,[64-66] the potential role of defects
447 on their transport behavior need to be refined based on the latest advances in membrane
448 characterization. The respective roles of the nodular layer and the exterior layer need to
449 be further resolved with respect to the transport of both water and solutes. Better
450 characterization methods are also needed for studying the nanosized defects and voids
451 within the PA layer as well as for the accurate determination of the effective membrane
452 transport area. Furthermore, some existing characterization results may need to be
453 reassessed to determine whether their interpretation could be affected by the presence
454 of these nanosized features (e.g., pore size measurement of RO membranes based on
455 the rejection of sugar molecules[67, 68] and position annihilation lifetime spectroscopy[56]).
456
457 The current study also implies the critical importance of optimizing of the ultrathin
458 selective PA skin. A key challenge would be to prepare a thin yet defect-free PA skin
459 with large SAR in order to overcome the upper-bound tradeoff[6, 59, 60] of PA membranes.
460 This in turn calls for the careful optimization of the reaction recipes and the interfacial
461 degassing conditions to promote the growth of thin polyamide films with larger
462 filtration area and to avoid extensive defects formation at the same time. One highly

promising method is the including of an interlayer[69-71] between the PA and the substrate layers, which enhances water permeability and minimizes defects formation simultaneously.

Supporting Information

The Supporting Information is available free of charge on the ACS Publications website at DOI:

S1. Membrane performance tests; S2. The impact of NaOCl treatment on the PSF substrate; S3. FESEM micrographs of the exterior features of XLE and NF90; S4. Determination of nodule size; S5. Determination of the apparent and intrinsic thicknesses by TEM; S6. Determination of SAR value using TEM micrographs; S7. Fe(II) tracer filtration test from the backside of BW30; S8. HA tracer filtration tests from the frontside of BW30 and NF90; S9. FESEM observation of the defective nodular layer of NF90; S10. XPS elemental composition of the frontside and backside of isolated PA layers; S11. Effect of DMF treatment on PA morphology

Acknowledgement

This research was funded by the National Key R&D Program of China (No. 2017YFC0403903), the National Natural Science Foundation of China (No. 21706231), and the Seed Funding for Strategic Interdisciplinary Research Scheme, the University of Hong Kong. Aromem Pte. Ltd. (Suzhou, China) is kindly acknowledged for providing free PSF substrate samples.

References

1. Elimelech, M.; Phillip, W. A., The future of seawater desalination: Energy, technology, and the environment. *Science* **2011,** *333*, (6043), 712.
2. Tang, C. Y.; Yang, Z.; Guo, H.; Wen, J. J.; Nghiem, L. D.; Cornelissen, E., Potable Water Reuse through Advanced Membrane Technology. *Environmental Science & Technology* **2018,** *52*, (18), 10215-10223.
3. Ridgway, H. F.; Orbell, J.; Gray, S., Molecular simulations of polyamide membrane materials used in desalination and water reuse applications: Recent developments and future prospects. *J. Membr. Sci.* **2017,** *524*, 436-448.
4. Cadotte, J. E., Evolution of composite reverse osmosis membranes. In *Materials Science of Synthetic Membranes*, American Chemical Society: 1985; Vol. 269, pp 273-294.
5. Petersen, R. J., Composite reverse osmosis and nanofiltration membranes. *J. Membr. Sci.* **1993,** *83*, (1), 81-150.
6. Yang, Z.; Guo, H.; Tang, C. Y., The upper bound of thin-film composite (TFC) polyamide membranes for desalination. *Journal of Membrane Science* **2019,** *590*, 117297.
7. Kim, S. H.; Kwak, S.-Y.; Suzuki, T., Positron annihilation spectroscopic evidence to demonstrate the flux-enhancement mechanism in morphology-controlled Thin-Film-Composite (TFC) membrane. *Environ. Sci. Technol.* **2005,** *39*, (6), 1764-1770.
8. Pacheco, F. A.; Pinnau, I.; Reinhard, M.; Leckie, J. O., Characterization of isolated polyamide thin films of RO and NF membranes using novel TEM techniques. *J. Membr. Sci.* **2010,** *358*, (1), 51-59.
9. Freger, V., Nanoscale heterogeneity of polyamide membranes formed by interfacial polymerization. *Langmuir* **2003,** *19*, (11), 4791-4797.
10. Kurihara, M.; Hanakawa, M., Mega-ton water system: Japanese national research and development project on seawater desalination and wastewater reclamation. *Desalination* **2013,** *308*, 131-137.
11. Jeong, B.-H.; Hoek, E. M. V.; Yan, Y.; Subramani, A.; Huang, X.; Hurwitz, G.; Ghosh, A. K.; Jawor, A., Interfacial polymerization of thin film nanocomposites: A new concept for reverse osmosis membranes. *J. Membr. Sci.* **2007,** *294*, (1), 1-7.
12. Pacheco, F. A., Microscopic characterization of the nanostructure of polyamide thin films in reverse osmosis and nanofiltration membranes. *Ph.D. Thesis. Stanford University* **December 2011**.
13. Freger, V., Kinetics of film formation by interfacial polycondensation. *Langmuir* **2005,** *21*, (5), 1884-1894.
14. Freger, V., Swelling and morphology of the skin layer of polyamide composite membranes: An atomic force microscopy study. *Environ. Sci. Technol.* **2004,** *38*, (11), 3168-3175.
15. Lin, L.; Feng, C.; Lopez, R.; Coronell, O., Identifying facile and accurate methods to measure the thickness of the active layers of thin-film composite membranes – A

529 comparison of seven characterization techniques. *J. Membr. Sci.* **2016,** *498*, 167-179.
530 16. Pacheco, F.; Sougrat, R.; Reinhard, M.; Leckie, J. O.; Pinnau, I., 3D visualization
531 of the internal nanostructure of polyamide thin films in RO membranes. *J. Membr. Sci.*
532 **2016,** *501*, 33-44.
533 17. Yan, H.; Miao, X.; Xu, J.; Pan, G.; Zhang, Y.; Shi, Y.; Guo, M.; Liu, Y., The porous
534 structure of the fully-aromatic polyamide film in reverse osmosis membranes. *J. Membr.*
535 *Sci.* **2015,** *475*, 504-510.
536 18. Lin, L.; Lopez, R.; Ramon, G. Z.; Coronell, O., Investigating the void structure of
537 the polyamide active layers of thin-film composite membranes. *J. Membr. Sci.* **2016,**
538 *497*, 365-376.
539 19. Song, X.; Smith, J. W.; Kim, J.; Zaluzec, N. J.; Chen, W.; An, H.; Dennison, J. M.;
540 Cahill, D. G.; Kulzick, M. A.; Chen, Q., Unraveling the Morphology–Function
541 Relationships of Polyamide Membranes Using Quantitative Electron Tomography. *ACS*
542 *Applied Materials & Interfaces* **2019,** *11*, (8), 8517-8526.
543 20. Kłosowski, M. M.; McGilvery, C. M.; Li, Y.; Abellan, P.; Ramasse, Q.; Cabral, J.
544 T.; Livingston, A. G.; Porter, A. E., Micro-to nano-scale characterisation of polyamide
545 structures of the SW30HR RO membrane using advanced electron microscopy and
546 stain tracers. *Journal of Membrane Science* **2016,** *520*, 465-476.
547 21. Culp, T. E.; Shen, Y.-x.; Geitner, M.; Paul, M.; Roy, A.; Behr, M. J.; Rosenberg, S.;
548 Gu, J.; Kumar, M.; Gomez, E. D., Electron tomography reveals details of the internal
549 microstructure of desalination membranes. *Proceedings of the National Academy of*
550 *Sciences* **2018,** *115*, (35), 8694-8699.
551 22. Li, Y.; Kłosowski, M. M.; McGilvery, C. M.; Porter, A. E.; Livingston, A. G.;
552 Cabral, J. T., Probing flow activity in polyamide layer of reverse osmosis membrane
553 with nanoparticle tracers. *Journal of Membrane Science* **2017,** *534*, 9-17.
554 23. Ma, X.-H.; Yao, Z.-K.; Yang, Z.; Guo, H.; Xu, Z.-L.; Tang, C. Y.; Elimelech, M.,
555 Nanofoaming of polyamide desalination membranes to tune permeability and
556 selectivity. *Environmental Science & Technology Letters* **2018,** *5*, (2), 123-130.
557 24. Kong, C.; Kanezashi, M.; Yamomoto, T.; Shintani, T.; Tsuru, T., Controlled
558 synthesis of high performance polyamide membrane with thin dense layer for water
559 desalination. *J. Membr. Sci.* **2010,** *362*, (1), 76-80.
560 25. Yan, W.; Shi, M.; Wang, Z.; Zhao, S.; Wang, J., Confined growth of skin layer for
561 high performance reverse osmosis membrane. *J. Membr. Sci.* **2019,** *585*, 208-217.
562 26. Karan, S.; Jiang, Z.; Livingston, A. G., Sub-10 nm polyamide nanofilms with
563 ultrafast solvent transport for molecular separation. *Science* **2015,** *348*, (6241), 1347-
564 1351.
565 27. Jiang, Z.; Karan, S.; Livingston, A. G., Water transport through ultrathin polyamide
566 nanofilms used for reverse osmosis. *Adv. Mater.* **2018,** *30*, (15), 1705973.
567 28. Lee, J.; Hill, A.; Kentish, S., Formation of a thick aromatic polyamide membrane
568 by interfacial polymerisation. *Sep. Purif. Technol.* **2013,** *104*, 276-283.
569 29. Shen, H.; Wang, S.; Xu, H.; Zhou, Y.; Gao, C., Preparation of polyamide thin film
570 nanocomposite membranes containing silica nanoparticles via an in-situ polymerization
571 of SiCl4 in organic solution. *J. Membr. Sci.* **2018,** *565*, 145-156.
572 30. Song, X.; Gan, B.; Yang, Z.; Tang, C. Y.; Gao, C., Confined nanobubbles shape the

surface roughness structures of thin film composite polyamide desalination membranes. *Journal of Membrane Science* **2019,** *582*, 342-349.
31. Ma, X.; Yang, Z.; Yao, Z.; Guo, H.; Xu, Z.; Tang, C. Y., Tuning roughness features of thin film composite polyamide membranes for simultaneously enhanced permeability, selectivity and anti-fouling performance. *Journal of Colloid and Interface Science* **2019,** *540*, 382-388.
32. Peng, L. E.; Yao, Z.; Liu, X.; Deng, B.; Guo, H.; Tang, C. Y., Tailoring polyamide rejection layer with aqueous carbonate chemistry for enhanced membrane separation: Mechanistic insights, chemistry-structure-property relationship, and environmental implications. *Environ. Sci. Technol.* **2019,** *53*, (16), 9764-9770.
33. Song, X.; Qi, S.; Tang, C. Y.; Gao, C., Ultra-thin, multi-layered polyamide membranes: Synthesis and characterization. *Journal of Membrane Science* **2017,** *540*, 10-18.
34. Xu, J.; Yan, H.; Zhang, Y.; Pan, G.; Liu, Y., The morphology of fully-aromatic polyamide separation layer and its relationship with separation performance of TFC membranes. *J. Membr. Sci.* **2017,** *541*, 174-188.
35. Yan, W.; Wang, Z.; Zhao, S.; Wang, J.; Zhang, P.; Cao, X., Combining co-solvent-optimized interfacial polymerization and protective coating-controlled chlorination for highly permeable reverse osmosis membranes with high rejection. *J. Membr. Sci.* **2019,** *572*, 61-72.
36. Hirose, M.; Ito, H.; Kamiyama, Y., Effect of skin layer surface structures on the flux behaviour of RO membranes. *J. Membr. Sci.* **1996,** *121*, (2), 209-215.
37. Tan, Z.; Chen, S.; Peng, X.; Zhang, L.; Gao, C., Polyamide membranes with nanoscale Turing structures for water purification. *Science* **2018,** *360*, (6388), 518.
38. Shen, L.; Hung, W.-s.; Zuo, J.; Zhang, X.; Lai, J.-Y.; Wang, Y., High-performance thin-film composite polyamide membranes developed with green ultrasound-assisted interfacial polymerization. *J. Membr. Sci.* **2019,** *570-571*, 112-119.
39. Wong, M. C. Y.; Lin, L.; Coronell, O.; Hoek, E. M. V.; Ramon, G. Z., Impact of liquid-filled voids within the active layer on transport through thin-film composite membranes. *J. Membr. Sci.* **2016,** *500*, 124-135.
40. Fujioka, T.; Oshima, N.; Suzuki, R.; Price, W. E.; Nghiem, L. D., Probing the internal structure of reverse osmosis membranes by positron annihilation spectroscopy: Gaining more insight into the transport of water and small solutes. *J. Membr. Sci.* **2015,** *486*, 106-118.
41. Mi, B.; Eaton, C. L.; Kim, J.-H.; Colvin, C. K.; Lozier, J. C.; Mariñas, B. J., Removal of biological and non-biological viral surrogates by spiral-wound reverse osmosis membrane elements with intact and compromised integrity. *Water Research* **2004,** *38*, (18), 3821-3832.
42. Hornstra, L. M.; Rodrigues Da Silva, T.; Blankert, B.; Heijnen, L.; Beerendonk, E.; Cornelissen, E. R.; Medema, G., Monitoring the integrity of reverse osmosis membranes using novel indigenous freshwater viruses and bacteriophages. *Environmental Science: Water Research and Technology* **2019,** *5*, (9), 1535-1544.
43. Slipko, K.; Reif, D.; Wögerbauer, M.; Hufnagl, P.; Krampe, J.; Kreuzinger, N., Removal of extracellular free DNA and antibiotic resistance genes from water and

wastewater by membranes ranging from microfiltration to reverse osmosis. *Water Res.* **2019,** *164*, 114916.
44. Fujioka, T.; Boivin, S., Assessing the passage of particles through polyamide reverse osmosis membranes. *Sep. Purif. Technol.* **2019,** *226*, 8-12.
45. Kwon, Y.-N.; Shih, K.; Tang, C.; Leckie, J. O., Adsorption of perfluorinated compounds on thin-film composite polyamide membranes. *Journal of Applied Polymer Science* **2012,** *124*, (2), 1042-1049.
46. Tang, C. Y.; Kwon, Y.-N.; Leckie, J. O., Probing the nano- and micro-scales of reverse osmosis membranes—A comprehensive characterization of physiochemical properties of uncoated and coated membranes by XPS, TEM, ATR-FTIR, and streaming potential measurements. *J. Membr. Sci.* **2007,** *287*, (1), 146-156.
47. Tang, C. Y.; Kwon, Y.-N.; Leckie, J. O., Effect of membrane chemistry and coating layer on physiochemical properties of thin film composite polyamide RO and NF membranes: II. Membrane physiochemical properties and their dependence on polyamide and coating layers. *Desalination* **2009,** *242*, (1), 168-182.
48. Do, V. T.; Tang, C. Y.; Reinhard, M.; Leckie, J. O., Degradation of polyamide nanofiltration and reverse osmosis membranes by hypochlorite. *Environmental Science & Technology* **2012,** *46*, (2), 852-859.
49. Cuperus, F. P.; Bargeman, D.; Smolders, K., A new method to determine the skin thickness of asymmetric UF-membranes using colloidal gold particles. *Journal of Colloid And Interface Science* **1990,** *135*, (2), 486-495.
50. Avena, M. J.; Koopal, L. K.; van Riemsdijk, W. H., Proton Binding to Humic Acids: Electrostatic and Intrinsic Interactions. *J. Colloid Interface Sci.* **1999,** *217*, (1), 37-48.
51. Dai, R.; Guo, H.; Tang, C. Y.; Chen, M.; Li, J.; Wang, Z., Hydrophilic selective nanochannels created by metal organic frameworks in nanofiltration membranes enhance rejection of hydrophobic endocrine-disrupting compounds. *Environmental Science & Technology* **2019,** *53*, (23), 13776-13783.
52. Yip, N. Y.; Tiraferri, A.; Phillip, W. A.; Schiffman, J. D.; Elimelech, M., High performance thin-film composite forward osmosis membrane. *Environ. Sci. Technol.* **2010,** *44*, (10), 3812-3818.
53. Kurihara, M.; Sasaki, T.; Nakatsuji, K.; Kimura, M.; Henmi, M., Low pressure SWRO membrane for desalination in the mega-ton water system. *Desalination* **2015,** *368*, 135-139.
54. Shi, M.; Wang, Z.; Zhao, S.; Wang, J.; Zhang, P.; Cao, X., A novel pathway for high performance RO membrane: Preparing active layer with decreased thickness and enhanced compactness by incorporating tannic acid into the support. *J. Membr. Sci.* **2018,** *555*, 157-168.
55. Ma, X.-H.; Yang, Z.; Yao, Z.-K.; Guo, H.; Xu, Z.-L.; Tang, C. Y., Interfacial polymerization with electrosprayed microdroplets: Toward controllable and ultrathin polyamide membranes. *Environmental Science & Technology Letters* **2018,** *5*, (2), 117-122.
56. Fujioka, T.; O'Rourke, B. E.; Michishio, K.; Kobayashi, Y.; Oshima, N.; Kodamatani, H.; Shintani, T.; Nghiem, L. D., Transport of small and neutral solutes through reverse osmosis membranes: Role of skin layer conformation of the polyamide

661 film. *J. Membr. Sci.* **2018,** *554*, 301-308.
662 57. Tang, C. Y.; Kwon, Y.-N.; Leckie, J. O., Fouling of reverse osmosis and
663 nanofiltration membranes by humic acid—Effects of solution composition and
664 hydrodynamic conditions. *J. Membr. Sci.* **2007,** *290*, (1), 86-94.
665 58. Coronell, O.; Mariñas, B. J.; Cahill, D. G., Depth heterogeneity of fully aromatic
666 polyamide active layers in reverse osmosis and nanofiltration membranes. *Environ. Sci.*
667 *Technol.* **2011,** *45*, (10), 4513-4520.
668 59. Geise, G. M.; Park, H. B.; Sagle, A. C.; Freeman, B. D.; McGrath, J. E., Water
669 permeability and water/salt selectivity tradeoff in polymers for desalination. *J. Membr.*
670 *Sci.* **2011,** *369*, (1), 130-138.
671 60. Park, H. B.; Kamcev, J.; Robeson, L. M.; Elimelech, M.; Freeman, B. D.,
672 Maximizing the right stuff: The trade-off between membrane permeability and
673 selectivity. *Science* **2017,** *356*, (6343), eaab0530.
674 61. Yao, Z.; Guo, H.; Yang, Z.; Lin, C.; Zhu, B.; Dong, Y.; Tang, C. Y., Reactable
675 substrate participating interfacial polymerization for thin film composite membranes
676 with enhanced salt rejection performance. *Desalination* **2018,** *436*, 1-7.
677 62. Li, X.; Li, Q.; Fang, W.; Wang, R.; Krantz, W. B., Effects of the support on the
678 characteristics and permselectivity of thin film composite membranes. *J. Membr. Sci.*
679 **2019,** *580*, 12-23.
680 63. Ramon, G. Z.; Wong, M. C. Y.; Hoek, E. M. V., Transport through composite
681 membrane, part 1: Is there an optimal support membrane? *J. Membr. Sci.* **2012,** *415-*
682 *416*, 298-305.
683 64. Spiegler, K. S.; Kedem, O., Thermodynamics of hyperfiltration (reverse osmosis):
684 criteria for efficient membranes. *Desalination* **1966,** *1*, (4), 311-326.
685 65. Urama, R. I.; Mariñas, B. J., Mechanistic interpretation of solute permeation
686 through a fully aromatic polyamide reverse osmosis membrane. *Journal of Membrane*
687 *Science* **1997,** *123*, (2), 267-280.
688 66. Coronell, O.; Mi, B.; Mariñas, B. J.; Cahill, D. G., Modeling the Effect of Charge
689 Density in the Active Layers of Reverse Osmosis and Nanofiltration Membranes on the
690 Rejection of Arsenic(III) and Potassium Iodide. *Environmental Science & Technology*
691 **2013,** *47*, (1), 420-428.
692 67. Nghiem, L. D.; Schäfer, A. I.; Elimelech, M., Removal of natural hormones by
693 nanofiltration membranes: Measurement, modeling, and mechanisms. *Environ. Sci.*
694 *Technol.* **2004,** *38*, (6), 1888-1896.
695 68. Yang, L.; She, Q.; Wan, M. P.; Wang, R.; Chang, V. W. C.; Tang, C. Y., Removal of
696 haloacetic acids from swimming pool water by reverse osmosis and nanofiltration.
697 *Water Research* **2017,** *116*, 116-125.
698 69. Yang, Z.; Zhou, Z.-w.; Guo, H.; Yao, Z.; Ma, X.-h.; Song, X.; Feng, S.-P.; Tang, C.
699 Y., Tannic Acid/Fe3+ Nanoscaffold for Interfacial Polymerization: Toward Enhanced
700 Nanofiltration Performance. *Environmental Science & Technology* **2018,** *52*, (16),
701 9341-9349.
702 70. Zhou, Z.; Hu, Y.; Boo, C.; Liu, Z.; Li, J.; Deng, L.; An, X., High-performance thin-
703 film composite membrane with an ultrathin spray-coated carbon nanotube interlayer.
704 *Environ. Sci. Technol. Lett.* **2018,** *5*, (5), 243-248.

71. Yang, X.; Du, Y.; Zhang, X.; He, A.; Xu, Z.-K., Nanofiltration membrane with a mussel-inspired interlayer for improved permeation performance. *Langmuir* **2017,** *33*, (9), 2318-2324.